Received: 3 February 2021 | Revised: 24 April 2021 | Accepted: 26 April 2021

DOI: 10.1002/mrm.28847

FULL PAPER

Magnetic Resonance in Medicine

Effects of motion and retrospective motion correction on the visualization and quantification of perivascular spaces in ultrahigh resolution T2-weighted images at 7T

Xiaopeng Zong[1,2] | **Soham Nanavati**[3,4] | **Sheng-Che Hung**[1,2] | **Tengfei Li**[1,2] | **Weili Lin**[1,2]

[1]Department of Radiology, University of North Carolina, Chapel Hill, North Carolina, USA

[2]Biomedical Research Imaging Center, University of North Carolina, Chapel Hill, North Carolina, USA

[3]Department of Statistics and Operations Research, University of North Carolina, Chapel Hill, North Carolina, USA

[4]Department of Biology, University of North Carolina, Chapel Hill, North Carolina, USA

Correspondence
Xiaopeng Zong, Department of Radiology, University of North Carolina, CB#7515 Chapel Hill, NC 27599, USA.
Email: zongxp@gmail.com

Funding information
NIH, Grant/Award Number: 5R21NS095027-02

Purpose: Motion can strongly affect MRI image quality and derived imaging measures. We studied the effects of motion and retrospective motion correction (MC) on the visualization and quantitative measures of the perivascular space and penetrating vessel (PVSV) complex, an essential part of the glymphatic system, on high-resolution T_2-weighted MRI images at 7T.

Methods: MC was achieved by adjusting k-space data based on head positions measured using fat navigator images. PVSV visibility and quantitative measures including diameter, volume fraction (VF), count, and contrast were compared between images with and without MC.

Results: Without MC, VF, and count decreased significantly with increasing head rotation. MC improved PVSV visualization in all cases with severe motion artifacts. MC decreased diameter in white matter (WM) and increased VF, count, and contrast in basal ganglia and WM. The changes of VF, count, and contrast after MC strongly correlated with motion severity. MC eliminated the significant dependences of VF and count on rotation and reduced the inter-subject variations of VF and count. The effect sizes of age and breathing gas effects on VF and count, and contrast increased in most cases after MC, while those on diameter exhibited inconsistent behavior.

Conclusions: Motion affects PVSV quantification without MC. MC improves PVSV visibility and increases the statistical power of detecting physiological PVSV VF, count, and contrast changes but may have limited benefits for increasing the power for detecting diameter changes.

KEYWORDS

age dependence, carbogen breathing, motion correction, perivascular spaces, ultrahigh resolution MRI

1 | INTRODUCTION

Perivascular spaces (PVSs) are pial lined and fluid filled spaces surrounding penetrating arterioles and venules in the brain. In the putamen of elderly human subjects, the PVS diameters are typically in the range of 0.13-0.96 mm, with the majority below 0.5 mm.[1] The lengths of MRI visible PVSs are typically in the range of 1-20 mm.[2] They are an essential pathway of the brain's glymphatic system, which plays an important role in clearing metabolic wastes from the brain.[3,4] Increased numbers of MRI-visible PVSs have been widely reported in patients with neurological diseases compared to healthy controls.[5-15] In addition, increased numbers of PVSs are also associated with higher risk of future cerebral small vessel disease,[16] stroke,[17,18] recurrence of transient ischemic attack,[19] cognitive decline,[16,20] and development of subdural fluid accumulation in mild traumatic brain injury patients,[21] suggesting that PVS imaging may have prognostic values.

The PVS and enclosed blood vessels often cannot be resolved in the MRI images due to limited spatial resolution. Physiological changes in both PVS and blood vessels can affect the apparent PVS signals.[22] Therefore, in this paper, we will refer to the combined structure of PVSs and enclosed blood vessels as PVSVs. The number of MRI-visible PVSVs increases with age.[22,23] However, there are large inter-subject variations in the number of MRI-visible PVSVs in healthy subjects, potentially resulting in insufficient statistical power for detecting disease-related changes. Monitoring the longitudinal changes of PVSV morphology may alleviate the large inter-subject variations and provide new insight into the causal relationship between PVS enlargement and the occurrence of neurological disorders.

Image artifacts induced by motion are commonly observed in MRI images, especially in high-resolution ones, which require a relatively long scan time. The effects of motion artifacts on measured PVSV parameters remain poorly understood. Understanding the effects of motion is important because head motion may be different between patient groups and between time points for the same subject,[24] which may confound experimental findings. Motion correction (MC) techniques have not been applied for imaging PVSV, and the effects of MC on measured PVSV parameters are unknown. MC can potentially reduce motion artifacts and ensure consistent image quality across subjects and time points, thus increasing the statistical power for future studies.

In this paper, we investigate the effects of motion and retrospective MC on PVSV visualization and quantification in ultrahigh resolution T_2 weighted images, which can visualize a large number (~450-2300) of PVSVs in the brain in young to middle-aged healthy subjects.[22] The head motion was monitored continuously during the scan by acquiring fat navigator images (FatNavs) every 3 s.[25]

2 | METHODS

2.1 | Subjects

This study was approved by the Institutional Review Board of the University of North Carolina at Chapel Hill. Thirty-nine healthy volunteers aged 21-55 were included in the study. Written informed consents were obtained from all subjects before the scan. All underwent MRI scans while breathing air, while 32 of them additionally underwent scans while breathing carbogen (5% carbon dioxide and 95% oxygen). Further details about the experimental setup can be found in a recent paper.[22]

2.2 | Data acquisition

All images were acquired using a 7T MRI scanner (Siemens Healthineer, Erlangen, Germany) equipped with a Nova 32-channel receiver and 8-channel transmitter head coil (Nova Medical, Wilmington, MA, USA). No radio frequency magnetic field (B_1) shimming was performed. A 3D variable flip angle turbo spin echo (TSE) sequence was used to image PVSVs.[2,26] The sequence parameters were as follows: TR/TE = 3000/326 ms, partial Fourier factor = 0.79 and 0.625 along the phase encoding (PE) and partition encoding (PAR) directions, respectively, echo train length = 859 ms, GRAPPA factor = 3 with 24 auto-calibration lines along PE direction, field of view (FOV) = 210 × 210 × 99.2 mm^3, matrix size= 512 × 525 × 248, oversampling factor 3.23% along PAR, voxel size = 0.41 × 0.4 × 0.4 mm^3, axial slices, scan time = 8:03 min. Each echo train acquired k-space data for one PAR step.

3D FatNavs[25] were acquired within each TR to monitor head motion. The navigator images had a voxel size = 2.2 × 2.2 × 2.2 mm^3 and were acquired during the idle period (=2.1 s) between echo trains. The fat signal excitation was centered at 3.4 ppm upfield from water. The sequence parameters were: TR/TE = 3.1/1.5 ms, flip angle = 7°, GRAPPA factors = 4 × 4, FOV = 220 × 220 × 180 mm^3, matrix size = 100 × 100 × 82, voxel size = 2.2 × 2.2 × 2.2 mm^3, axial slices, partial Fourier factor = 0.75 along both the phase and partition encoding directions, duration = 0.89 s. A navigator image was also acquired before the first TR which included fully sampled GRAPPA calibration data from a 32 × 20 (PE × PAR) rectangular region centered at k-space center. The total duration of the first navigator image was 2.75 s.

2.3 | Data analysis

2.3.1 | Fat image reconstruction

The FatNavs were reconstructed using the standard GRAPPA reconstruction algorithm after inverse Fourier transform

(IFT) of the data along the readout direction.[27] A separate kernel with a size of 2 × 2 was estimated for each position along the readout to calculate the missing k-space data. The missing data due to partial Fourier acquisition were zero filled before IFT along PAR and PE to obtain single channel images. The images from all channels were combined into a single image by root mean square.

2.3.2 | Motion parameters

The series of navigator images in each scan were registered to the 129th image in the series using the 3dvolreg tool in AFNI.[28] The 129th image was chosen as the k-space center was measured during that repetition. Motion ranges, defined as the differences of the maximum and minimum values of the six rigid-body motion parameters, were calculated. The rotational and translational motion ranges were then combined by root sum square to obtain the total rotational (M_R) and translational motions (M_T), respectively. Furthermore, to quantify the seemingly random fast fluctuations of motion parameters, the time series of each motion parameter was fitted with a fifth order polynomial to estimate the slow drift of head position and the residual standard deviation (rSD) after the fit were calculated. Visual inspection found that a fifth order polynomial was adequate to model the slow changes of motion parameters during the scan.

2.3.3 | Water image reconstruction

To study the effects of MC on PVSV parameters, the TSE images based on water proton signal were reconstructed both with and without MC (NoMC). The following steps were carried out to reconstruct the NoMC images: (1) IFTs were first applied along the readout and PAR directions, after zero-filling missing data due to partial Fourier acquisition; (2) GRAPPA reconstruction was performed with a separate kernel of size 4 for each grid point in the readout–PAR plane; (3) IFTs were then performed along the PE direction; (4) the images from all the channels were combined into a single image by root mean square. To obtain MC images, the above IFT in step (3) was replaced by nonuniform IFT as follows[29]: (1) Fourier transforms were performed along the readout and PAR directions to convert the data back into the k-space; (2) the k-space coordinates of the readout–PE plane at each PAR step were adjusted based on the three rotational motion parameters estimated for the corresponding TR; (3) linear phase shifts were applied to the k-space data to correct for translational motion; (4) the k-space data were then transformed back to the image space by nonuniform IFT with the same spatial resolution as the NoMC images using a nonuniform FFT toolbox.[30]

2.3.4 | PVSV parameters

We used the mono channel version of a fully convoluted neural network[31] to delineate the PVSV masks. For simplicity, only the original reconstructed images were used as input to the network and the auto-contextual information from the probability maps was not used for refinement. From the masks, we identified spatially connected clusters that had more than one voxel. Then, a one-voxel thick path connecting two terminal voxels was defined for each cluster. Voxels belonging to a path were labelled as VoP and the apparent diameter (D_{VoP}) was calculated for each VoP. To investigate the potential brain region dependence of the motion artifacts, we calculated mean D_{VoP}, count, contrast, and volume fraction (VF) in two regions of interest (ROI): white matter (WM) and basal ganglia (BG). Mean diameter was calculated by averaging D_{VoP} over all VoPs in an ROI. VF was calculated as the fraction of ROI voxels occupied by PVSVs. Count was defined as the number of PVSV clusters that intersected with an ROI. PVSVs that intersected with both WM and BG were assigned to the ROI that contained the most voxels from such PVSVs. Contrast was calculated as $2\left(S_{pvs} - S_t\right) / \left(S_{pvs} + S_t\right)$, where S_{pvs} and S_t are the mean signals of the PVSVs and a one-voxel thick layer of surrounding tissue, respectively. Details of VoP, and D_{VoP} determinations and the process for obtaining WM and BG ROIs can be found in our earlier study.[22] We also calculated the standard deviation (SD) of voxel intensities in a background ROI normalized by the mean intensity of the same ROI (SD_{norm}) to assess the noise characteristics. The background ROI was defined as a 15.6 × 15.6 × 15.6 mm^3 cube outside the skull at the corner of the field of view. We note that in our earlier studies,[2,22] instead of contrast, relative contrast-to-noise ratio (rCNR) was quantified which used the mean signal in the background ROI to estimate the noise. However, rCNR will be different from that in those studies because of the difference in coil combination method (root mean square here versus adaptive combination in earlier studies).

2.3.5 | Visual evaluation

Images were first evaluated by a neuroradiologist (S.H.) who had 19 y of experience and was blinded to the reconstruction of images. For each scan, MC and NoMC images were randomly renamed as images 1 and 2, respectively and then SH determined whether image 1 was better than, similar to, or worse than image 2, based on PVSV sharpness in bilateral frontal and parietal WM and basal ganglia. In addition, images were also visually evaluated by a second rater (X.Z.) who had 12 y of experience in brain MRI research but was aware of the reconstruction method for each image, to evaluate the artifact levels which included blurring of gray

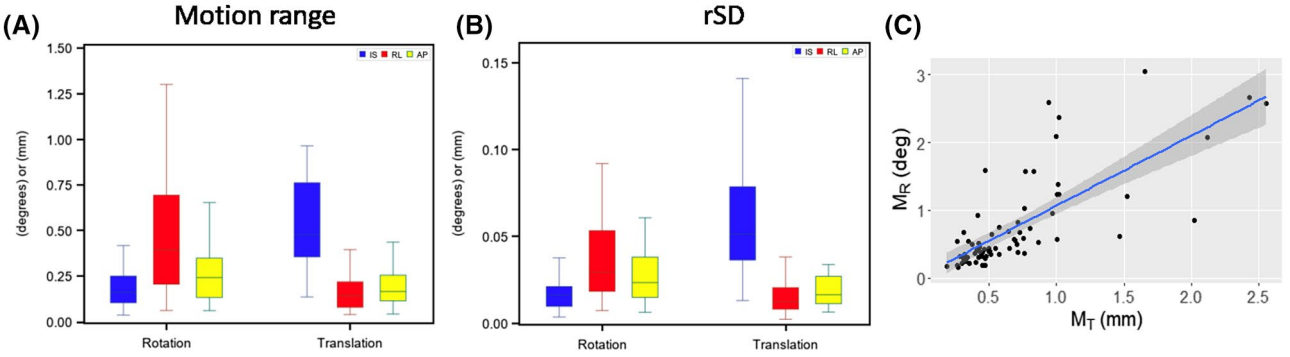

FIGURE 1 A, Ranges of translational and rotational motions along the AP, RL, and IS directions. B, Residual standard deviations after fifth order polynomial fit of the translational and rotational motion parameters. C, Scatter plot of M_T versus M_R, showing a high degree of correlation between them

matter (GM)-WM boundary, blurring of PVSV, and ripples in NoMC images and to assess the reduction of the artifact levels after MC. To facilitate the comparison of artifact levels between MC and NoMC images, we registered an MC image to the NoMC image of the same scan using the flirt tool in FSL.[32] Nearest neighbor interpolation was used to avoid smoothing of brain structures in the registered MC images. Then the NoMC and registered MC images were visually compared at the same slice position for artifact levels.

2.3.6 | Statistical analysis

To test whether there was significant difference in motion range and rSD between the three (right-left (RL), anterior-posterior (AP), and inferior-superior (IS)) spatial dimensions, Welch's analysis of variance (ANOVA) tests were performed and, for tests that showed significant difference, post-hoc Game-Howell tests were performed to identify the pairs that had significant difference.

To study the dependences of PVSV parameters on motion, multivariate linear regression analyses were performed using age, gender, gas condition, and M_T or M_R as independent variables. Only one of the two motion parameters (M_T or M_R) was included in the analysis as they were highly correlated to each other as will be shown below.

Wilcoxon's signed rank tests were performed to evaluate the significances of the differences between PVSV parameters with MC and NoMC. To evaluate whether MC reduced the inter-subject variations of PVSV parameters, regression analyses were performed using age, gender, gas condition as independent variables. Residual coefficients of variation (rCV) after regression were calculated to compare the differences of rCV between NoMC and MC.

To study whether MC increased the statistical powers for detecting age and breathing gas-dependent changes of PVSV parameters, the same statistical analyses as in our earlier study[22] were carried out. Specifically, linear regression analyses were performed using age and gender as independent variables for PVSV parameters under air breathing to study age effects. Wilcoxon's signed rank tests were performed to compare the PVSV parameters between air and carbogen breathing in subjects who underwent both air and carbogen scans. Furthermore, effect sizes (ESs) were employed as an index of statistical power and compared between NoMC and MC. For the age coefficients, the ES was defined as the ratio between the fitted values and the product of their standard errors and the square root of subject number ($n = 39$). For the differences between carbogen and air, the ES was defined as the ratio between the mean and standard deviation of the difference ($n = 32$). To estimate the errors of the ES differences between NoMC and MC, the following bootstrapping procedure was performed: (1) the subjects were randomly sampled with replacement to generate new groups with the same number of subjects; (2) the ESs of the new groups were calculated using the same procedure as described above; (3) the random sampling was repeated 100 times and the SDs of the ES differences between NoMC and MC among the 100 repetitions were calculated; (4) z scores were calculated as the ratio between the ES difference in the real data and the estimated SD and corresponding *P*-values (two-tailed) were obtained from the z scores. p-values were adjusted by Bonferroni correction to account for double tests in the two ROIs and adjusted p-values less than 0.05 were considered significant.

3 | RESULTS

3.1 | Motion characteristics

The total rotational and translational motions ranged from 0.2° to 3.1° (mean ± SD = 0.8° ± 0.7°), and 0.2 to 2.6 mm (0.7 ± 0.5 mm), respectively. Figure 1A shows the motion ranges along the IS, RL, and AP directions, showing significant difference between the three directions ($P \leq 1.2 \times$

10^{-5}, Welch's ANOVA tests). The range of rotational motion around RL was significantly larger than around IS and AP ($P \leq 0.0009$, Games-Howell test), while not significantly different between IS and AP. On the other hand, the translational motion range was significantly greater along IS than along RL and AP ($P \leq 0.0007$, Games-Howell test), while not significantly different between RL and AP.

Figure 1B displays the rSD of the motion parameters after regressing out the gradual head motion with fifth-order polynomial fitting. Among all cases, the maximum rSDs for rotation and translation were 0.37° around the RL axis, and 0.22 mm along IS, respectively. The mean ± SD of rSDs for rotations around IS, RL, and AP axes were 0.02° ± 0.02°, 0.06° ± 0.07°, and 0.03° ± 0.02°, respectively, while the mean rSDs for translation along IS, RL, and AP were 0.06 ± 0.04 mm, 0.002 ± 0.01 mm, and 0.02 ± 0.02 mm.

There was a strong correlation (Pearson's R = 0.75, $P = 2.3 \times 10^{-14}$) between the rotational and translational motions, as shown in Figure 1C.

3.2 | Visual evaluation of image artifacts

The first rater, who was blinded to the image reconstruction method found that the image qualities of the MC images were superior, similar, and inferior to the NoMC images in 47, 21, and 3 cases, respectively. The M_T ranges in the three groups were 0.3-2.6 mm, 0.2-1.5 mm, and 0.3-0.4 mm, respectively, while the M_R ranges were 0.2-3.1°, 0.2-1.2°, and 0.30-0.33°.

Visual evaluation by the second rater in the NoMC images found severe artifacts in 20 (27%) cases. Two examples of images with severe motion artifacts are shown in the left panels of Figure 2A,B. The artifacts of GM − WM boundary blurring, PVSV blurring, and ripples are denoted by the arrowhead, solid, and hollow arrows, respectively. Motion traces for the same images are provided in Figure 3A,B, showing translation of ~1 mm and/or rotation of ~1°. The left panel of Figure 4A is an example NoMC image with almost no visible artifacts. The total translation and rotation were only ~0.2 mm and 0.2°, respectively, as shown in Figure 4B. All the 20 cases with severe artifacts had $M_T \geq 0.8$ mm and/or $M_R \geq 0.83°$, which will thereafter be referred to as large motion.

Large motion was also present in four other cases, although, motion artifacts were less apparent in those images. Inspection of the motion parameter time courses of the four cases revealed that the large motion was caused by one or two spikes in three of the cases, suggesting that such spikes did not have strong effect on the overall image quality. However, in the remaining case, the time course showed more gradual variations throughout the scan. Reinspection of this case found localized shaded bands in the brain. Representative slices and the motion parameter time courses of this and the other three cases can be found in Supporting Information Figures S1 and S2, which are available online, respectively.

NoMC and MC images were visually compared side by side after registration. Improved PVSV visibility including reduced blurring and increased contrast were observed in all the 20 cases with severe artifacts, consistent with the rating by the radiologist. Two examples of increased PVSV visibility after MC are shown in the right panels of Figure 2A,B, where PVSV contrast was higher and blurring was reduced. On the other hand, when the amount of motion was small, the appearances of PVSVs were similar between MC and NoMC images in all cases, as shown in the example in Figure 4A. However, we noticed increased ripples in the WM after MC in six of the cases with severe motion artifacts including the example image in Figure 2A where the ripples were denoted by the hollow arrows. No increased ripples were observed in any other cases.

Among the four cases with large motion but mild motion artifacts, improved PVSV visibility was observed only in one case (the case with gradual motion) but remained

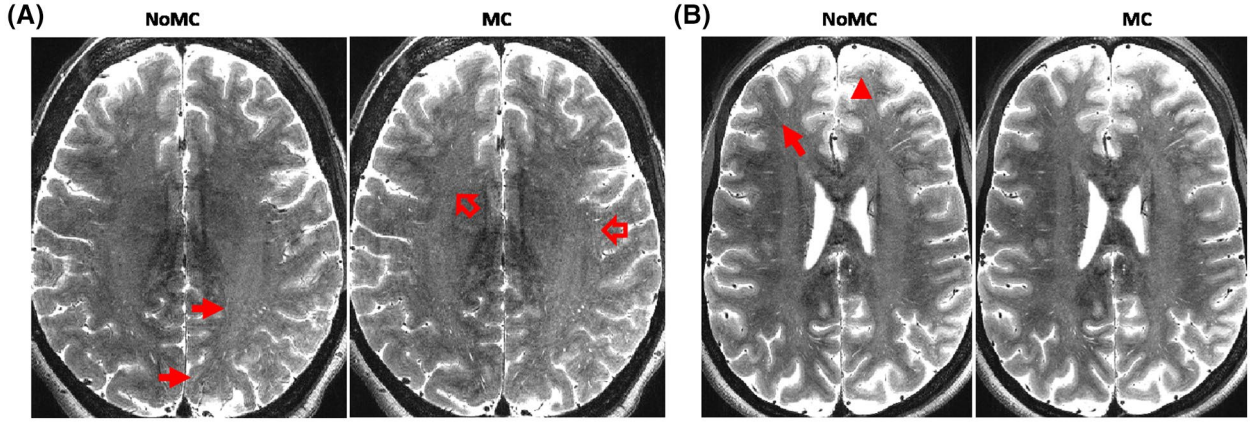

FIGURE 2 Reconstructed images without and with MC in two representative subjects with large motion. The solid arrows, arrow heads, and hollow arrows denote blurring of PVSV, blurring of GM – WM boundary, and ripples within brain, respectively. The blurring of GM – WM boundary and PVSV are more severe in the NoMC images while the ripples are more severe in the MC image

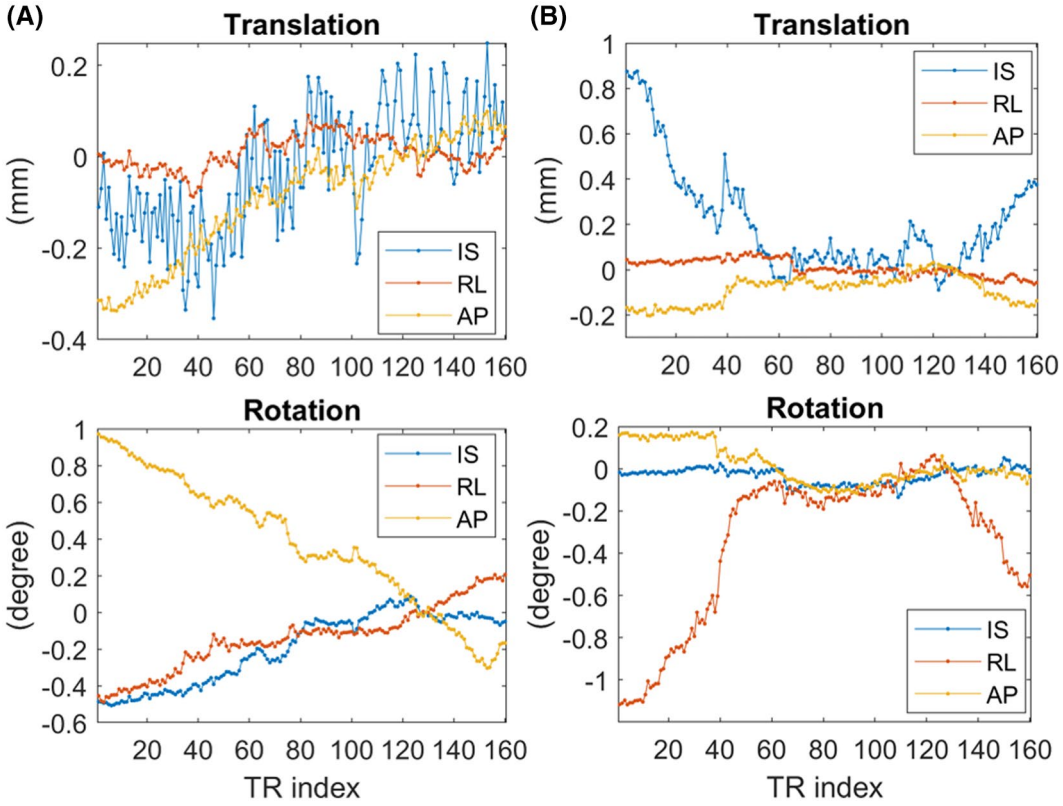

FIGURE 3 A, B, The motion parameter time courses for the images shown in Figure 2A,B, respectively

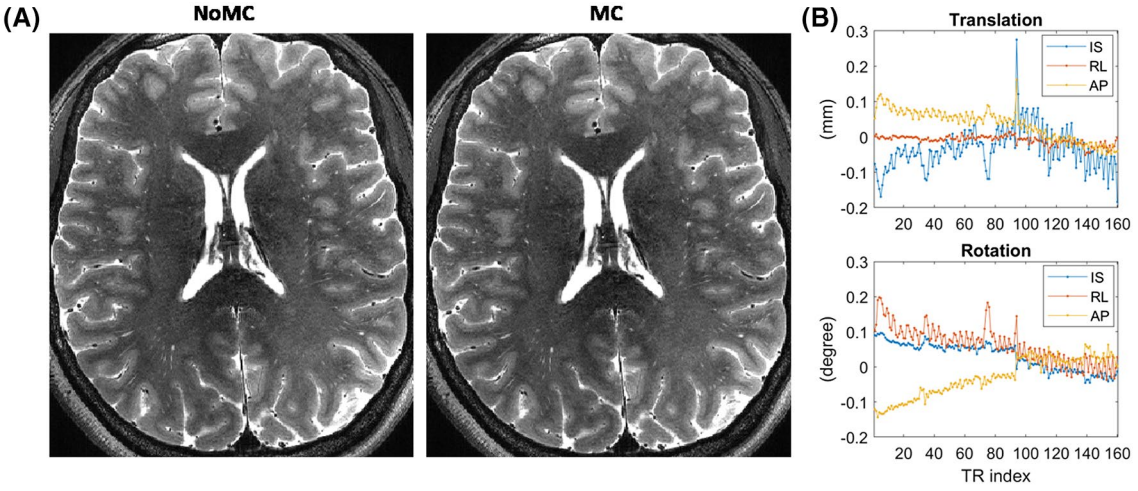

FIGURE 4 A, The reconstructed images without and with MC for a scan with small motion. No clear change in artifact level was observed between MC and NoMC. B, The motion parameter time courses for the same scan

similar in the other three cases by the second rater. However, all the four cases were rated as improved after MC by the radiologist.

Overall, the agreements between the two raters for the cases with and without severe artifacts were 100% and 43%, respectively. If we assess whether or not MC reduced image quality by combining the ratings of "better" and "similar" into one category, then the agreement for the cases without severe artifacts became 94%.

3.3 | Quantitative comparison between MC and NoMC

Quantitative comparison of PVSV parameters between MC and NoMC are shown in Figure 5. Each parameter was normalized by the corresponding group average with NoMC. VF, count, and contrast were significantly increased after MC in both WM and BG (corrected $P \leq 2.9 \times 10^{-3}$, Wilcoxon's signed rank test). In addition, the diameter decreased by 2.2%

after MC in WM (corrected $P \leq 3.8 \times 10^{-10}$). The group averages of the PVSV parameters and the percent changes after MC are given in Supporting Information Table S1.

3.4 | Correlation between motion and PVSV parameters

With NoMC, VF in WM (corrected $P = .012$) and count in BG and WM (corrected $P \leq 0.034$) were significantly dependent on M_R, after regressing out age, gender, and breathing gas effects. With MC, the dependences of VF and count on M_R or M_T were no longer significant. No significant dependence on M_R or M_T was found for contrast and diameter, regardless of whether MC was applied. The coefficients of M_T and M_R in the regression analyses are given in Supporting Information Table S2.

On the other hand, the differences of VF, count, and contrast between MC and NoMC showed strong positive correlations (corrected $P \leq .026$) with M_T and M_R, as shown in Figure 6. However, the diameter changes were not significantly correlated with M_T or M_R. The slopes of the PVSV parameter differences versus M_T and M_R are listed in Supporting Information Table S3.

The SD_{norm} in the background ROI decreased after MC. With NoMC, SD_{norm} was not significantly correlated with M_T or M_R ($P \geq .60$; Spearman's correlation test). However, after MC, SD_{norm} showed strong negative correlation with M_T and M_R ($P \leq 01.3 \times 10^{-7}$; Spearman's correlation test). The scatter plots of SD_{norm} versus M_T and M_R can be found in Supporting Information Figure S3.

3.5 | Inter-subject variations after MC

There were large residual inter-subject variations (rCV values = 0.24-0.51) in VF and count with NoMC, after regressing out age, gender, and gas effects. After MC, the rCV values were reduced for both VF and count. On the hand, there were almost no changes in rCVs for diameter and contrast. The rCV values are listed in Table 1.

3.6 | Statistical powers of detecting age and gas effects

3.6.1 | Age effect

In the linear regression analyses, the age coefficients for VF, count, and contrast in BG, but none of the other parameters, were significantly different from zero, regardless of whether MC was performed. For further comparison between MC and NoMC, the ESs of the age coefficients are shown in Figure 7. The ESs increased after MC in most cases, except for the diameter and count in BG. However,

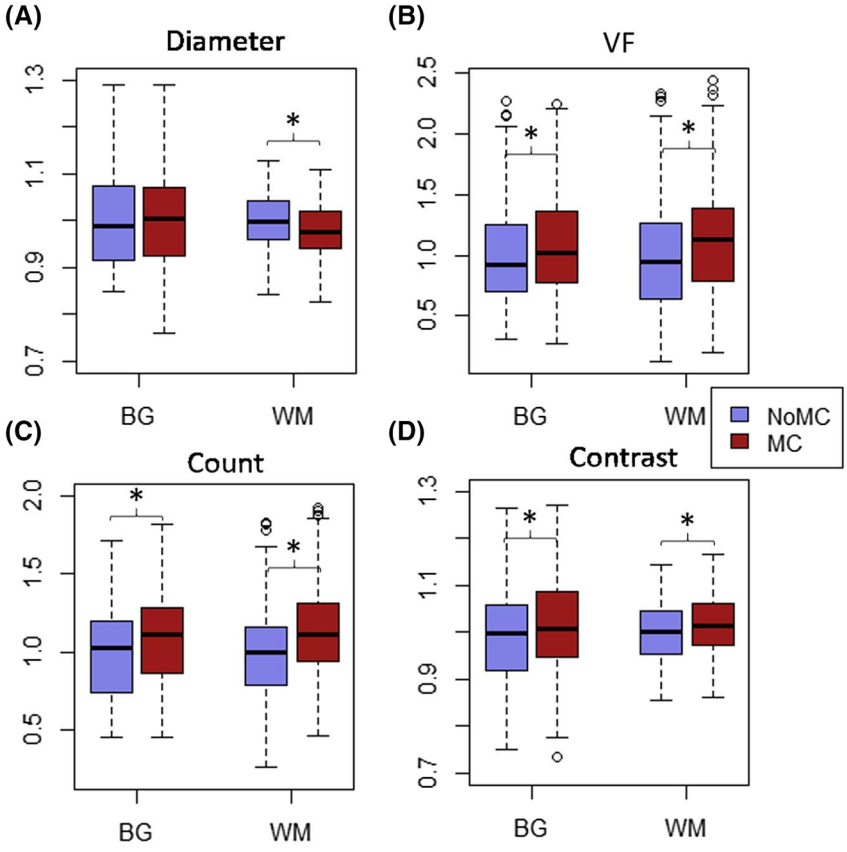

FIGURE 5 Boxplots of PVSV diameter (A), VF (B), count (C), and contrast (D) in BG and WM. Before plotting, all values were normalized by the corresponding group averages with NoMC. The asterisks denote significant difference between MC and NoMC (corrected $P < .05$) using a Wilcoxon's signed rank test

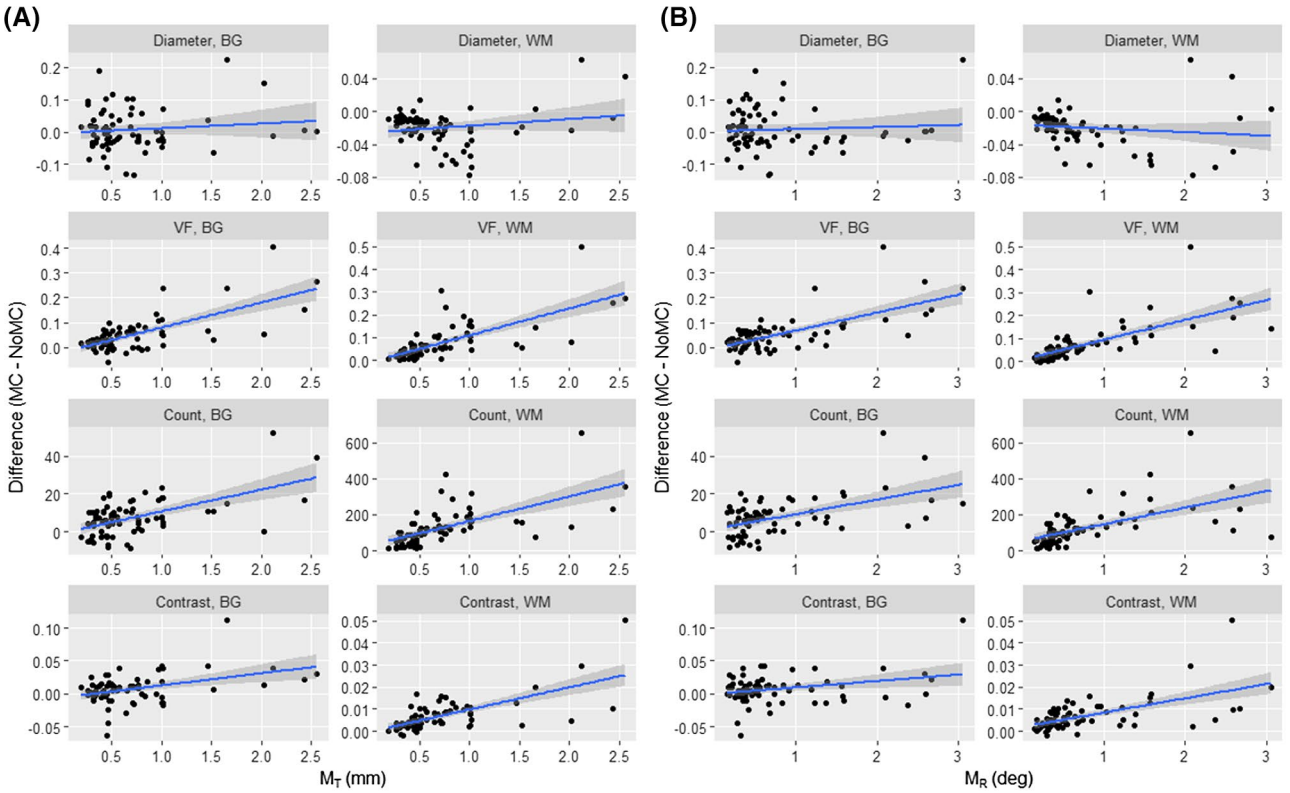

FIGURE 6 Scatter plots of the differences in PVSV diameter (first row), VF (second row), count (third row), and contrast (fourth row) between MC and NoMC versus M_T (A) and M_R (B)

	BG			WM		
Parameter	**NoMC**	**MC**	**Change**	**NoMC**	**MC**	**Change**
Diameter	0.10	0.11	0.01	0.07	0.07	0.00
VF	0.32	0.28	−0.04	0.51	0.44	−0.06
Count	0.24	0.21	−0.03	0.34	0.30	−0.05
Contrast	0.10	0.09	−0.01	0.065	0.064	−0.001

TABLE 1 Residual coefficients of variation in multivariate linear regression analyses of PVSV parameters with age, gender, and gas condition as independent variables[a]

[a]The third column of each ROI gives the differences between MC and NoMC.

none of the differences in ESs between MC and NoMC reached significance after Bonferroni correction (corrected $P \geq .82$). The fitted values and standard errors of all age coefficients can be found in Supporting Information Table S4.

3.6.2 | Gas effect

Significant gas effects were observed in VF and count only after MC. On the other hand, gas effect on diameter and contrast was significant in WM with both MC and NoMC. The ESs of the carbogen breathing-induced changes in PVSV parameters are shown in Figure 8. The ESs of diameter and contrast showed inconsistent changes in the two ROIs. After MC, the ESs of count and contrast significantly increased in WM but that of diameter significantly decreased in BG.

To further study the source of ES changes after MC, the mean and standard errors of the carbogen-induced parameter changes are listed in Table 2. Table 2 shows that the increased ESs of VF and count after MC can be attributed to both increased means and decreased SDs. On the other hand, both the means and SDs of diameter and contrast decreased after MC.

4 | DISCUSSION

In this paper, we studied the effects of motion and retrospective MC on PVSV parameters. We found that (1) MC increased the visualization of PVSV in all images with severe

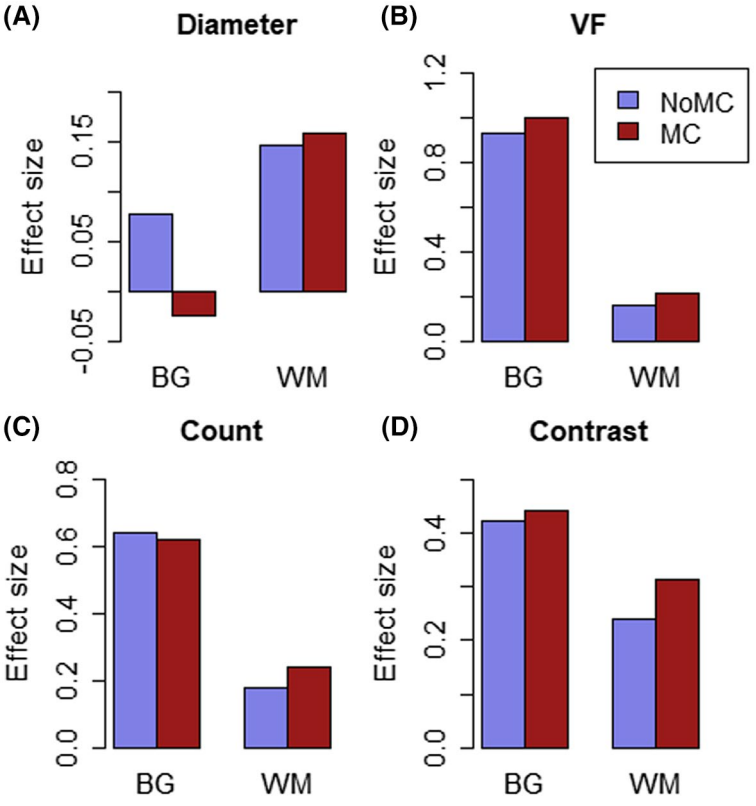

FIGURE 7 Effect sizes of the age coefficients in the regression analyses of PVSV diameter (A), VF (B), count (C), and contrast (D) in BG and WM under air breathing using age and gender as independent variables

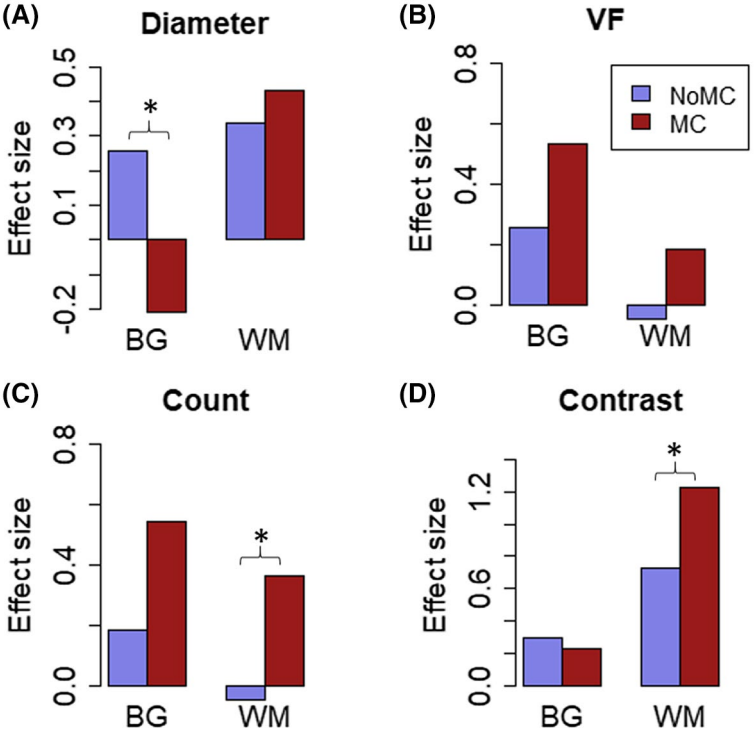

FIGURE 8 Effect sizes of the differences between carbogen and air breathing for PVSV diameter (A), VF (B), count (C), and contrast (D) in BG and WM. The asterisks denote significant difference between MC and NoMC (corrected $P \leq .03$)

motion artifacts. (2) MC decreased PVSV diameter in WM and increased VF, count, and contrast in both BG and WM; (3) PVSV count and VF were affected by rotation when no MC was applied and MC removed such effects; (4) The differences of VF, count, and contrast between MC and NoMC were strongly correlated with the amount of motion; (5) MC reduced the residual inter-subject variations of VF and count; and (6) the ESs of age and gas effects on VF, count, and contrast increased after MC in most cases, but the ES changes were inconsistent for diameter.

TABLE 2 The mean (SD) of the differences of PVSV parameters between carbogen and air breathing[a]

	NoMC		MC	
Parameter	**BG**	**WM**	**BG**	**WM**
D (mm)	0.02 (0.08)	0.014 (0.042)*	−0.017 (0.079)	0.008 (0.018)*
VF (%)	0.034 (0.14)	−0.01 (0.18)	0.04 (0.08)*	0.02 (0.09)*
Count	3 (18)	−8 (171)	7 (12)*	29 (80)
Contrast	0.01 (0.04)	0.011 (0.014)*	0.006 (0.026)	0.009 (0.008)*

[a]The asterisks denote values that are significantly different from zero after Bonferroni correction using Wilcoxon's signed rank tests.

While both raters agreed on the improvements of PVSV visibility by MC in all cases with severe motion artifacts, the agreement was only 43% in other cases. This can be explained by the smaller differences between the MC and NoMC images when motion artifacts were mild or absent. However, in 94% of such cases, both raters agreed that MC did not reduce PVSV visibility. Therefore, MC is a reliable method for improving PVSV visibility in cases of severe artifacts while still preserving the visibility when such artifacts are mild or absent.

We found that the head tended to rotate more around the LR axis and translate more along the IS direction. Both are consistent with the fact that there was less physical constraint for such movements. We tried to quantify the fluctuations of the measured motion parameters using rSD. In addition to noises, the rSD had contributions from fitting errors caused by real spike-like and stepwise changes in the time courses which cannot be fitted accurately. Therefore, rSD represents an upper limit of the random fluctuations. The small rSDs (mean values $\leq$0.06 mm and 0.06°) suggest that the FatNavs can provide highly precise measurement of head positions, consistent with earlier studies.[29] We note that the rSDs do not reflect the accuracy because of potential systematic errors in the motion parameters.

The associations of count and VF with M_R without MC suggest that, when comparing the PVSV parameters between groups or across time points, the potential confounding effects of head motion should be considered to ascertain the intrinsic differences. Navigator-based MC can reduce such confounding effects, as shown by the removal of such associations after MC. Interestingly, a strong correlation between SD_{norm} and motion parameters were observed after MC, suggesting that the rCNR as defined in our earlier studies[22] might not be a useful parameter after MC. The reason underlying the association between SD_{norm} and motion after MC remains unknown. One possibility is an increased width of the point spread function (PSF) when the k-space sampling positions deviate from a cartesian grid, which could introduce spatial smoothing.

The PVSV diameter with MC were significantly smaller than that without MC in WM, which can be explained by a reduction of motion-induced blurring of PVSVs in the images. However, the diameters were similar between MC and NoMC in BG, which can be attributed to the larger PVSV diameters in BG, such that the blurring effect was not as prominent as in WM. On the other hand, the VF, count, and contrast were greater with MC than those with NoMC in most subjects, and the difference correlated strongly with the degree of motion. The decreased diameter and larger increase of VF than count after MC (Supporting Information Table S1) suggest that the lengths of visualized PVSVs increased after MC, likely due to the visualization of longer PVSV segments near the ends of PVSVs which are often thinner than the middle part.[2] Two factors might have contributed to the larger PVSV count and VF after MC. First, MC increased the visibility of PVSV in the presence of severe motion because of the increased contrast, which was further supported by the visual rating by the radiologist blinded to the reconstruction method. In addition, the segmentation algorithm may have higher sensitivity in images with MC, since it was trained using images without severe motion artifacts. In cases with severe motion, the PVSV appearance with MC became more similar to those encountered during training than that without MC, leading to higher PVSV segmentation sensitivity with MC.

We found that MC reduced the inter-subject variations in PVSV count and VF, suggesting that varying degrees of motion artifacts in different subjects contributed to such variations. Therefore, MC can also be helpful for increasing the statistical powers of detecting intrinsic PVSV parameter changes by reducing inter-subject variations. This was further supported by the fact that significant carbogen-induced VF and count changes were observed only after MC. Further, the ESs of VF, count, and contrast increased after MC in most cases (Figures 7 and 8), although most did not reach statistical significance.

We note that the significances of the age and gas effects on PVSV parameters with NoMC are mostly consistent with our previous findings,[22] except for the age dependence of contrast and carbogen-induced VF changes, both of which were significant in BG and WM in the previous study.[22] The difference might be explained by the exclusion of subjects with severe motion artifacts and inclusion of five additional

subjects for whom no navigator images were acquired in that study. With MC, the significance of carbogen-induced VF changes was recovered in both ROIs. The carbogen-induced count increase also became significant in BG, which was not significant in Ref. 22.

It is interesting to note that the ripple artifact was more severe after MC in 6 of the 20 cases where there were severe motion artifacts. One possible cause of the increased ripple artifact is the inherent errors in the motion parameters. In some subjects, apparent oscillations in the motion parameters were observed, as can be seen for the translation along IS in Figure 3A. Such oscillations might be caused by B_0 field fluctuations due to subject breathing but not by real head motion. Correcting for such artificial head motion could, thus, result in increased ripple artifacts. The source of the apparent oscillations in motion parameters and filtering techniques to remove them need to be further studied in the future.

Our study has several limitations. First, only retrospective MC was studied and no reacquisition of motion corrupted data were performed. Therefore, the full benefits of MC may not be realized in the MC images. Prospective MC may further improve PVSV visualization and ensure consistent image quality among subjects. Second, the retrospective image reconstruction method might be further improved. In our study, GRAPPA reconstruction was performed before MC. Algorithms that can directly reconstruct images based on non-Cartesian k-space data should be explored. Third, B_1 inhomogeneity might have reduced the PVSV contrast and VF in brain regions with low B_1, such as close to the brain surface.[2,33]

5 | CONCLUSIONS

In conclusion, we found that PVSV VF and count decreased with increasing head rotation without MC. Retrospective MC based on FatNavs improved the visibility of PVSV in subjects with large motion. MC significantly increased the count, VF, and contrast in BG and WM, and decreased the diameter in WM. The MC-induced increases in count, VF, and contrast were strongly correlated with the range of motion. Furthermore, MC reduced the residual inter-subject variations in PVSV count and VF and increased the ESs of VF, count, and contrast for detecting age and breathing gas-dependent changes. However, the benefit of MC for improving the statistical power of diameter changes may be limited.

ACKNOWLEDGMENTS

This study was partly supported by the United States NIH grant 5R21NS095027-02. We thank the reviewers for their valuable suggestions for improving the manuscript.

DATA AVAILABILITY STATEMENT

The MATLAB code for image reconstruction can be downloaded from http://dx.doi.org/10.17632/4vt7bw97f3.1. The raw data can be provided upon signing a formal data sharing agreement.

ORCID

Xiaopeng Zong https://orcid.org/0000-0003-4235-6948

TWITTER

Xiaopeng Zong @zongxp

REFERENCES

1. Pesce C, Carli F. Allometry of the perivascular spaces of the putamen in aging. *Acta Neuropathol*. 1988;76:292-294.
2. Zong X, Park SH, Shen D, et al. Visualization of perivascular spaces in the human brain at 7T: sequence optimization and morphology characterization. *Neuroimage*. 2016;125:895-902.
3. Iliff JJ, Wang M, Liao Y, et al. A paravascular pathway facilitates CSF flow through the brain parenchyma and the clearance of interstitial solutes, including amyloid beta. *Sci Transl Med*. 2012;4:147ra111.
4. Rasmussen MK, Mestre H, Nedergaard M. The glymphatic pathway in neurological disorders. *Lancet Neurol*. 2018;17:1016-1024.
5. Chen W, Song X, Zhang Y, et al. Assessment of the Virchow-Robin spaces in Alzheimer disease, mild cognitive impairment, and normal aging, using high-field MR imaging. *AJNR Am J Neuroradiol*. 2011;32:1490-1495.
6. Hansen TP, Cain J, Thomas O, et al. Dilated perivascular spaces in the Basal Ganglia are a biomarker of small-vessel disease in a very elderly population with dementia. *AJNR Am J Neuroradiol*. 2015;36:893-898.
7. Boespflug EL, Simon MJ, Leonard E, et al. Targeted assessment of enlargement of the perivascular space in Alzheimer's disease and vascular dementia subtypes implicates astroglial involvement specific to Alzheimer's disease. *J Alzheimers Dis*. 2018;66:1587-1597.
8. Cai K, Tain R, Das S, et al. The feasibility of quantitative MRI of perivascular spaces at 7T. *J Neurosci Methods*. 2015;256:151-156.
9. Kilsdonk ID, Steenwijk MD, Pouwels PJ, et al. Perivascular spaces in MS patients at 7 Tesla MRI: a marker of neurodegeneration? *Mult Scler*. 2015;21:155-162.
10. Wuerfel J, Haertle M, Waiczies H, et al. Perivascular spaces–MRI marker of inflammatory activity in the brain? *Brain*. 2008;131(Pt 9):2332-2340.
11. Inglese M, Bomsztyk E, Gonen O, Mannon LJ, Grossman RI, Rusinek H. Dilated perivascular spaces: hallmarks of mild traumatic brain injury. *AJNR Am J Neuroradiol*. 2005;26:719-724.
12. Doubal FN, MacLullich AMJ, Ferguson KJ, et al. Enlarged perivascular spaces on MRI are a feature of cerebral small vessel disease. *Stroke*. 2010;41:450-454.
13. Zhu Y-C, Tzourio C, Soumaré A, et al. Severity of dilated Virchow-Robin spaces is associated with age, blood pressure, and MRI markers of small vessel disease: a population-based study. *Stroke*. 2010;41:2483-2490.
14. Duperron M-G, Tzourio C, Sargurupremraj M, et al. Burden of dilated perivascular spaces, an emerging marker of cerebral small vessel disease, is highly heritable. *Stroke*. 2018;49:282-287.

15. Park YS, Chung MS, Choi BS. MRI assessment of cerebral small vessel disease in patients with spontaneous intracerebral hemorrhage. *Yonsei Med J*. 2019;60:774-781.
16. Ding J, Sigurðsson S, Jónsson PV, et al. Large perivascular spaces visible on magnetic resonance imaging, cerebral small vessel disease progression, and risk of dementia: the age gene/environment susceptibility-Reykjavik study. *JAMA Neurol*. 2017;74:1105-1112.
17. Duperron M-G, Tzourio C, Schilling S, et al. High dilated perivascular space burden: a new MRI marker for risk of intracerebral hemorrhage. *Neurobiol Aging*. 2019;84:158-165.
18. Gutierrez J, Elkind M, Dong C, et al. Brain perivascular spaces as biomarkers of vascular risk: results from the Northern Manhattan study. *AJNR Am J Neuroradiol*. 2017;38:862-867.
19. Lau K-K, Li L, Lovelock CE, et al. Clinical correlates, ethnic differences, and prognostic implications of perivascular spaces in transient ischemic attack and ischemic stroke. *Stroke*. 2017;48:1470-1477.
20. Park YW, Shin N-Y, Chung SJ, et al. Magnetic resonance imaging-visible perivascular spaces in Basal Ganglia predict cognitive decline in Parkinson's disease. *Mov Disord*. 2019;34:1672-1679.
21. Koo H-W, Oh M, Kang HK, et al. High-degree centrum semiovale-perivascular spaces are associated with development of subdural fluid in mild traumatic brain injury. *PLoS One*. 2019;14:e0221788.
22. Zong X, Lian C, Jimenez J, Yamashita K, Shen D, Lin W. Morphology of perivascular spaces and enclosed blood vessels in young to middle-aged healthy adults at 7T: dependences on age, brain region, and breathing gas. *Neuroimage*. 2020;218:116978.
23. Ishikawa M, Yamada S, Yamamoto K. Dilated perivascular spaces in the centrum semiovale begin to develop in middle age. *J Alzheimers Dis*. 2018;61:1619-1626.
24. Zeng L-L, Wang D, Fox MD, et al. Neurobiological basis of head motion in brain imaging. *Proc Natl Acad Sci*. 2014;111:6058.
25. Gallichan D, Marques JP, Gruetter R. Retrospective correction of involuntary microscopic head movement using highly accelerated fat image navigators (3D FatNavs) at 7T. *Magn Reson Med*. 2016;75:1030-1039.
26. Busse RF, Hariharan H, Vu A, et al. Fast spin echo sequences with very long echo trains: design of variable refocusing flip angle schedules and generation of clinical T2 contrast. *Magn Reson Med*. 2006;55:1030-1037.
27. Griswold MA, Jakob PM, Heidemann RM, et al. Generalized autocalibrating partially parallel acquisitions (GRAPPA). *Magn Reson Med*. 2002;47:1202-1210.
28. Cox RW. AFNI: software for analysis and visualization of functional magnetic resonance neuroimages. *Comput Biomed Res*. 1996;29:162-173.
29. Gallichan D, Marques JP. Optimizing the acceleration and resolution of three-dimensional fat image navigators for high-resolution motion correction at 7T. *Magn Reson Med*. 2017;77:547-558.
30. Fessler JA, Sutton BP. Nonuniform fast Fourier transforms using min-max interpolation. *IEEE Trans Signal Process*. 2003;51:560-574.
31. Lian C, Zhang J, Liu M, et al. Multi-channel multi-scale fully convolutional network for 3D perivascular spaces segmentation in 7T MR images. *Med Image Anal*. 2018;46:106-117.
32. Jenkinson M, Bannister P, Brady M, et al. Improved optimization for the robust and accurate linear registration and motion correction of brain images. *Neuroimage*. 2002;17:825-841.
33. Vaughan JT, Garwood M, Collins CM, et al. 7T vs. 4T: RF power, homogeneity, and signal-to-noise comparison in head images. *Magn Reson Med*. 2001;46:24-30.

SUPPORTING INFORMATION

Additional Supporting Information may be found online in the Supporting Information section.

FIGURE S1 Reconstructed images without MC in the subject that had mild artifacts and large motion that occurred gradually. The upper panel shows motion parameter time courses and the lower panel shows a representative axial image slice. Localized shading artifact can be observed as denoted by the red arrow

FIGURE S2 (A-C) reconstructed images without MC in the three subjects, respectively, that had mild artifacts and large motion caused by spikes in motion parameter time courses. The upper panels are motion parameter time course and the lower panels are representative axial image slices

FIGURE S3 Scatter plots of SD_{norm} versus (A) M_T and (B) M_R. The left and right panels are for results without and with MC, respectively

TABLE S1 Group averaged PVSP parameters with and without MC and their percent differences. The asterisks denote significant difference between MC and NoMC (corrected $P < .05$) using a Wilcoxon's signed rank test

TABLE S2 The coefficients for M_T and M_R in the multivariate linear regression analyses of PVSV parameters in NoMC and MC images, using age, gender, breathing gas, and M_T or M_R as independent variables. The asterisks denote coefficients that are significantly different from 0 (corrected $P < .05$). The numbers inside the parentheses are standard errors. The first and second units in the second column are for M_T and M_R coefficients, respectively

TABLE S3 Slopes of linear fits to the differences of PVSV parameters between MC and NoMC versus M_T or M_R. The asterisks denote slopes that are significantly different from 0 (corrected $P \leq 6.6 \times 10^{-6}$). The numbers inside the parentheses are standard errors. The first and second units in the first column are for M_T and M_R coefficients, respectively

TABLE S4 Coefficients (standard errors) of age in the linear regression analysis of PVSV parameters under air breathing using age and gender as independent variables. The asterisks denote values that are significantly different from zero after Bonferroni correction

How to cite this article: Zong X, Nanavati S, Hung S-C, Li T, Lin W. Effects of motion and retrospective motion correction on the visualization and quantification of perivascular spaces in ultrahigh resolution T2-weighted images at 7T. *Magn Reson Med*. 2021;86:1944–1955. https://doi.org/10.1002/mrm.28847